(Preprint) AAS 18-011

COMPARING COARSE SUN SENSOR BASED SEQUENTIAL SUN HEADING FILTERS

Thibaud Teil*, Hanspeter Schaub† and Scott Piggott ‡

In a sun heading determination scenario coarse sun-sensors (CSS) can be paired with rate gyros in order to estimate attitude and spacecraft rotation rate. These paired measurements allow for a fully observable state vector. However, relying solely on coarse sun-sensor measurements for sun heading and spacecraft rotation rate estimation is sometimes advantageous. Here the challenge is to find the most robust method for attitude determination without relying on rate gyros. In such a scenario, the rotation rate of the spacecraft can be estimated in order to provide state derivative control or simply for better sun heading estimation. Therefore, the state vector is traditionally the sun direction vector and its time derivative as seen by the body frame. This paper compares four different filters for gyro-less sun heading estimation. They vary in state vectors and kinematics, with the goal of controlling or removing non-observability. In order to compare the behavior of the set of sun-sensing algorithms, a modular filtering architecture is used and its utility is demonstrated. By incorporating this architecture in the Basilisk astrodynamics software package filter performances are compared through realistic scenarios.

INTRODUCTION

Coarse Sun-Sensors (CSSs) are small, relatively inexpensive, and regularly used for sunline heading determination. Cosine-type CSS devices output a voltage/current depending on the angle between the sensors normal and the sun direction. Although used in many micro and nano-satellite missions [1, 2], they are widely used in interplanetary missions including during safe-mode[3]. Previous work has efficiently used both rate gyros and CSS measurements [4], which allows for efficient attitude determination, notably in eclipse.

In contrast, it is often desirable to solely use sun heading for attitude determination. If the gyros are not sufficiently accurate, this allows for a more robust sensor to control attitude independently. Setting aside issues of observability, in a safe-mode scenario, it would also reduce the chances of using compromised measurements, and would reduce the additional sensors' associated power draw. With enough CSSs—traditionally two pyramids of four—a spacecraft can always have at least one activated CSS, and frequently several activated devices. The data can therefore be used for sun heading determination during normal spacecraft operations.

In the absence of rate gyros, it is preferable to estimate rate, both for better states estimation, and eventually for control. However, the desire to use CSS-only measurements for sun heading

*Graduate Research Assistant, Aerospace Engineering Sciences, University of Colorado Boulder

†Glenn L. Murphy Chair of Engineering, Department of Aerospace Engineering Sciences, University of Colorado, 431 UCB, Colorado Center for Astrodynamics Research, Boulder, CO 80309-0431. AAS Fellow.

‡ADCS Integrated Simulation Software Lead, Laboratory for Atmospheric and Space Physics, University of Colorado Boulder.

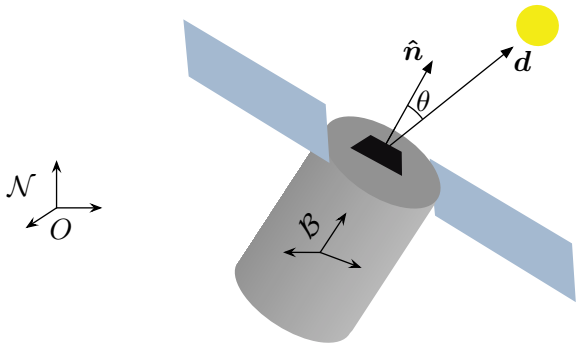

Figure 1. Spacecraft equipped with a CSS

determination exposes two observability issues. The first issue is that the spacecraft rotation rate's component about the sun heading direction is unobservable. In order to use it more reliably in safe-mode, there needs to be progress made on this front: notably by decoupling the unobservable component from the states and eventually observing it through novel methods.

The second challenge is due to the fact that, depending on the CSS field of view, the problem can suffer from a general lack of observability. Field of view here designates the cone in which each individual sensor can be activated. This un-observability is due to the nature of CSS measurements [5], as they only provide angular information between the sensor normal and the sun heading. This means that one CSS yields a cone of possibilities, two sensors lead to two sun direction possibilities, and only with three or more activated sensors do you get full observability instantaneously. If the sensors have a limited field of view, the spacecraft can go through time-spans with little information.

Given these two challenges, this paper attempts to develop a novel kinematic formulation for sun heading estimation. This formulation decouples the unobservable rate out of the state vector. In previous works such as Reference [6] and [7] the rate is not estimated by the filter. Combining this minimal and fully observable formulation with gyroscopic couplings as is done in Reference [8] could increase confidence when using sun heading filters during safe-mode.

In this paper, four filters are derived and their performances are compared. The first filter only estimates the sun heading vector, and computes a partial solution to the the satellite rotation rate at every step using the sun heading estimates. The second and third subtract the unobservable components out of the states in an Extended Kalman Filter (EKF) and a square-root unscented Kalman Filter (SR-uKF) respectively. In the final filter, the kinematics of the problem are reduced to a five-by-one vector estimating the sun direction and the observable rotation rate by tracking two different frames. This yields a state vector with no unobservable states. By switching between frames, the singularity can be avoided, and therefore presents a promising approach to decoupling one of the observability problems in these filters.

PROBLEM STATEMENT AND NOTATIONS

Scenario Description

This paper aims to analytically develop the four sequential estimators and compare their performance. To compare the filters, a scenario is created where a spacecraft is tumbling in deep space, and attempts to determine its sun heading direction and rotation rate vector.

Table 1. CSS Constellation

CSS Pyramid	${}^{\mathcal{B}}\hat{\boldsymbol{n}}_1$	${}^{\mathcal{B}}\hat{\boldsymbol{n}}_2$	${}^{\mathcal{B}}\hat{\boldsymbol{n}}_3$	${}^{\mathcal{B}}\hat{\boldsymbol{n}}_4$
1	$\left[\frac{\sqrt{2}}{2}, -0.5, 0.5\right]^T$	$\left[\frac{\sqrt{2}}{2}, -0.5, -0.5\right]^T$	$\left[\frac{\sqrt{2}}{2}, 0.5, 0.5\right]^T$	$\left[\frac{\sqrt{2}}{2}, 0.5, 0.5\right]^T$
2	$\left[-\frac{\sqrt{2}}{2}, -0.5, 0.5\right]^T$	$\left[-\frac{\sqrt{2}}{2}, -0.5, -0.5\right]^T$	$\left[-\frac{\sqrt{2}}{2}, 0.5, -0.5\right]^T$	$\left[-\frac{\sqrt{2}}{2}, 0.5, 0.5\right]^T$

The sun heading vector is estimated as a non-unit vector due to scale factors from the instruments [9]. The sun heading vector in the body frame is written ${}^{\mathcal{B}}\boldsymbol{d}$, its inertial derivative is $\dot{\boldsymbol{d}}$, and its body frame derivative is $\boldsymbol{d}'$. The direction cosine matrix from an arbitrary $\mathcal{S}$ frame into the spacecraft body frame $\mathcal{B}$ will be $[\mathcal{BS}]$, and the inertial frame is labeled $\mathcal{N}$. The filtering notation used complies with Chapter 4 of Referene 10, and the dynamics notation complies with Reference 11.

Observability

One way to quantify the observability of a plant, is to compute the observability Grammian. The rank of this matrix, determines the observability over a specified period of time: if it is full rank, the system is observable, if not, there are unobservable states in the system. In a discrete-continuous context, the equation for the Observability Grammian is given in Equation (1). In this equation, $[\Phi]$ represents the state transition matrix, and $[H]_k$ represents the linearized measurement model evaluated at step k.

$$\forall (n,m) \in \mathbb{N}, m < n, \qquad [G](t_m, t_n) = \sum_{t_k = t_m}^{t_n} [\Phi](t_k, t_m)^T [H]_k^T [H]_k [\Phi](t_k, t_m) \tag{1}$$

Throughout this paper, a double pyramid of four CSS devices each will be used. The normals for each of the sensors are displayed in Table 1 this allows a maximal sensor coverage. The field of view of each of these sensors will dictate the number of sensors that are activated for a specific attitude.

Figure 2 shows simultaneously the number of activated sensors, and the observability Grammian defined in Equation (1). The term "field of view" is used to describe the half-angle to the cone of visibility for each individual sensor. In the case where the sun sensors have a half-angle field of view of $60°$, seen in Figure 2(a), the Grammian is not always full rank. Since the rank value depends on the number of filter states, it is indicated with the red dotted line. For this plot, the sliding window used to compute the Grammian was of 10s, meaning $t_m - t_k = 10s$. Since the measurements are read at 2Hz, this sliding window used for the Grammian contains 20 measurements.This figure shows us that for a tumbling spacecraft there are several periods in which the states are not observable. This is corroborated by the coverage plot in Figure 3(a).

Nevertheless, fields of view can reach $85°$ with better quality sun-sensors and the results with this field of view can be seen in Figure 2(b) and 3(b). This leads to a much higher number of activated sun-sensors at every instant, as seen in Figure 2. The observability Grammian is nearly always full rank as the periods with only two activated CSS are brief, which is again corroborated by Figure 3(b).

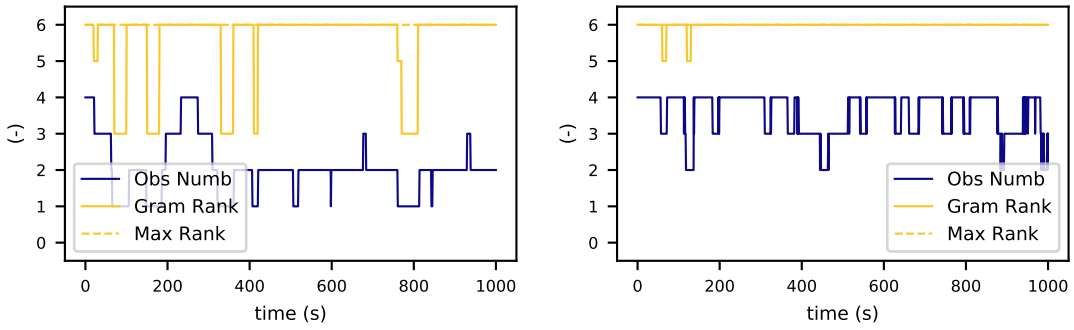

(a) CSS FOV of 60 °

(b) CSS FOV of 85 °

Figure 2. Rank of Observability Grammian and number of observations

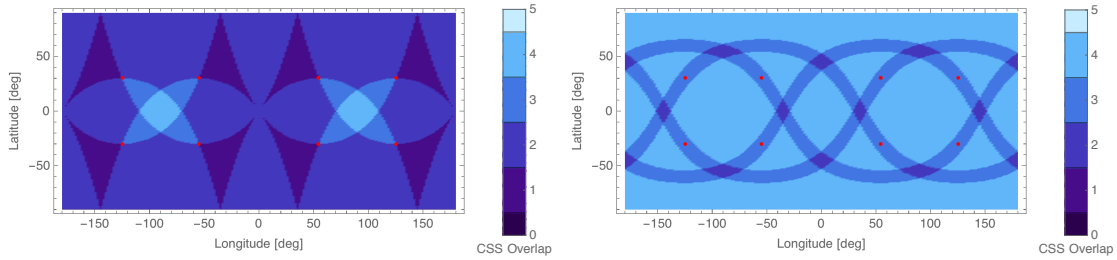

(a) CSS FOV of 60 °

(b) CSS FOV of 85 °

Figure 3. CSS coverage

Measurements

The measurement model is given in Equation (2), and the $[H]$ matrix defined as $[H] = \left[\frac{\partial \boldsymbol{G}(\boldsymbol{X},t_i)}{\partial \boldsymbol{X}}\right]^*$ is given in Equation (3). In these filters, the only measurements used are from the coarse sun sensors. For the i^{th} sensor, the measurement is simply given by the dot product of the sunline heading and the normal to the sensor:

$$\boldsymbol{G}_i(\boldsymbol{X}) = {}^{\mathcal{B}}\boldsymbol{n}_i \cdot {}^{\mathcal{B}}\boldsymbol{d} \tag{2}$$

This yields easy partial derivatives for the $[H]$ matrix:

$$[H](\boldsymbol{X}) = \begin{bmatrix} \boldsymbol{n}_1^T & [0_{1\times(n-3)}] \\ \vdots & \vdots \\ \boldsymbol{n}_i^T & [0_{1\times(n-3)}] \end{bmatrix} \tag{3}$$

where the rows contain the transposed normal vectors of the sensors that received measurements. Hence the $[H]$ matrix has a changing size depending on the amount of measurements. Additionally the size of $[H]$ matrix depends on the number of states as seen in Equation (3).

FILTER KINEMATICS AND DYNAMICS

In this section, the compared filters are described. The formulation of the dynamics is the main difference between all of these filters. The Extended Kalman Filter is derived in Reference [10].

Estimating only sun heading (Sunline-EKF)

The first filter is a standard sun heading filter EKF, which was developed to use rate gyro measurements if they are available [5]. In the case in which they are not, the rate is computed with the two previous sun heading estimates. The state vector of this filter only contains the sunline vector in body frame components: $\boldsymbol{X} = \begin{bmatrix}{}^{\mathcal{B}}\boldsymbol{d}\end{bmatrix}$. Given the nature of the filter, there is no unobservable state component as the inertial derivative of $\boldsymbol{d}$ is not estimated.

The propagation equation is given in Equation (4), and is discretized using an Euler integration in Equation (5).

$$\boldsymbol{X}' = \boldsymbol{F}(\boldsymbol{X}) = {}^{\mathcal{B}}\boldsymbol{d}' = -\boldsymbol{\omega}_{\mathcal{B}/\mathcal{N}} \times {}^{\mathcal{B}}\boldsymbol{d} = -[\tilde{\boldsymbol{\omega}}_{\mathcal{B}/\mathcal{N}}]{}^{\mathcal{B}}\boldsymbol{d} \tag{4}$$

$${}^{\mathcal{B}}\boldsymbol{d}_{k+1} = {}^{\mathcal{B}}\boldsymbol{d}_k - \Delta t \boldsymbol{\omega}_{\mathcal{B}/\mathcal{N}} \times {}^{\mathcal{B}}\boldsymbol{d}_k \tag{5}$$

This leads to the computation of the dynamics matrix $A = \left[\frac{\partial \boldsymbol{F}(\boldsymbol{X},t_i)}{\partial \boldsymbol{X}}\right]^*$. The partials are given in Equation (6).

$$[A] = \left[\frac{\partial \boldsymbol{F}(\boldsymbol{d},t_i)}{\partial \boldsymbol{d}}\right] = -\left[\tilde{\boldsymbol{\omega}}_{\mathcal{B}/\mathcal{N}}\right] \tag{6}$$

Because gyro measurements are not being read by the filter, they can be approximated [6, 7] by logging an extra time step of the sun heading vector estimate $\boldsymbol{d}$ given in Equation (7).

$$\boldsymbol{\omega}_k = \frac{1}{\Delta t}\frac{\boldsymbol{d}_k \times \boldsymbol{d}_{k-1}}{\|\boldsymbol{d}_k \times \boldsymbol{d}_{k-1}\|}\arccos\left(\frac{\boldsymbol{d}_k \cdot \boldsymbol{d}_{k-1}}{\|\boldsymbol{d}_k\|\|\boldsymbol{d}_{k-1}\|}\right) \tag{7}$$

Aliasing or noise issues can be predicted from such a formula. If the measurement times are too far apart with regard to the rate of change of the system, the rate may be poorly represented. On the other hand, if measurements are very close in time, the two vectors that are being crossed are nearly co-linear. This will lead to noise being amplified and the $\boldsymbol{\omega}$ value will not be representative either.

Subtracting un-observability (EKF)

The second filter derivation solves the rate un-observability by subtracting out the rate component along the sun heading axis out of the state. The states that are estimated in this filter are the sunline vector, and it's rate of change in the inertial frame $\boldsymbol{X} = \begin{bmatrix}{}^{\mathcal{B}}\boldsymbol{d} & {}^{\mathcal{B}}\boldsymbol{d}'\end{bmatrix}^T$.

The dynamics are given in Equation (8). Given the nature of the filter, there is an unobservable state component: the rotation about the $\boldsymbol{d}$ axis. In order to remedy this, the states are projected along this axis and subtracted, in order to measure only observable state components.

$$\boldsymbol{X}' = \boldsymbol{F}(\boldsymbol{X}) = \begin{bmatrix}\boldsymbol{F}_1(\boldsymbol{d}) \\ \boldsymbol{F}_2(\boldsymbol{d}')\end{bmatrix} = \begin{bmatrix}\boldsymbol{d}' - \left((\boldsymbol{d}\cdot\boldsymbol{d}')\frac{\boldsymbol{d}}{||\boldsymbol{d}||^2}\right) \\ -\frac{1}{\Delta t}\left((\boldsymbol{d}\cdot\boldsymbol{d}')\frac{\boldsymbol{d}}{||\boldsymbol{d}||^2}\right)\end{bmatrix} \tag{8}$$

This leads us to the computation of the dynamics matrix $A = \left[\frac{\partial \boldsymbol{F}(\boldsymbol{X},t_i)}{\partial \boldsymbol{X}}\right]^*$. The partials are given in Equation (9).

$$[A] = \begin{bmatrix}\frac{\partial \boldsymbol{F}_1(\boldsymbol{X},t_i)}{\partial \boldsymbol{d}} & \frac{\partial \boldsymbol{F}_1(\boldsymbol{X},t_i)}{\partial \boldsymbol{d}'} \\ \frac{\partial \boldsymbol{F}_2(\boldsymbol{X},t_i)}{\partial \boldsymbol{d}} & \frac{\partial \boldsymbol{F}_2(\boldsymbol{X},t_i)}{\partial \boldsymbol{d}'}\end{bmatrix} = \begin{bmatrix}-\left(\frac{\boldsymbol{d}'\boldsymbol{d}^T}{||\boldsymbol{d}||^2} + (\boldsymbol{d}\cdot\boldsymbol{d}')\frac{||\boldsymbol{d}||^2 I - 2\boldsymbol{d}\boldsymbol{d}^T}{||\boldsymbol{d}||^4}\right) & I - \frac{\boldsymbol{d}\boldsymbol{d}^T}{||\boldsymbol{d}||^2} \\ -\frac{1}{\Delta t}\left(\frac{\boldsymbol{d}'\boldsymbol{d}^T}{||\boldsymbol{d}||^2} + (\boldsymbol{d}\cdot\boldsymbol{d}')\frac{||\boldsymbol{d}||^2 I - 2\boldsymbol{d}\boldsymbol{d}^T}{||\boldsymbol{d}||^4}\right) & -\frac{1}{\Delta t}\frac{\boldsymbol{d}\boldsymbol{d}^T}{||\boldsymbol{d}||^2}\end{bmatrix} \tag{9}$$

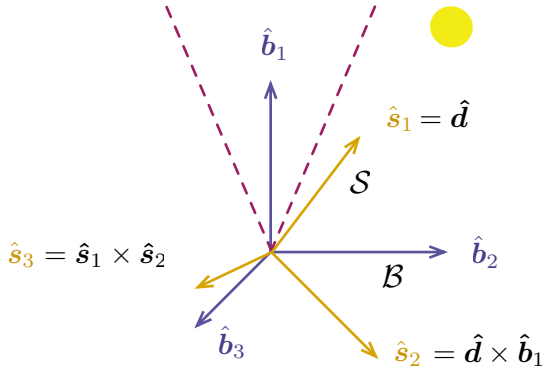

Figure 4. Frame built off the body frame for Switch-EKF

Subtracting un-observability (SR-uKF)

In order to implement another type of filter for state-estimation comparison, a square-root unsecented Kalman Filter [12] is implemented using the same formulation as the EKF. This filter has no need for partial derivative calculation, which does simplify code development given Equation (9).

This filter uses $\alpha = 0.02$ as a constant determining the spread of the sigma points. The prior knowledge of the probability distribution of the state is set with $\beta = 2$ (which is optimal for Gaussian distributions).

Switching frames (Switch-EKF)

Filter Derivation The final filter attempts to avoid subtracting any terms from the state, while still removing the unobservable component of the rate. In order to do this, an appropriate frame must be defined. In order to not track the rate component alongside the sunline direction, that vector needs to be one of the basis vectors of the frame. It is decided to be the first vector for the frame, and therefore in that frame, ω_1 the component of the rotation rate can be removed from the states. This frame is called $\mathcal{S}_1 = \{\hat{s}_1 = \frac{\boldsymbol{d}}{|\boldsymbol{d}|}, \hat{s}_2, \hat{s}_3\}$. This is seen in Figure 4, where the dotted line represents the 30° threshold cone before switching frames.

The second vector of the frame must be created using only $\boldsymbol{d}$, and the body frame vectors. The first intuitive decision, is to use $\hat{\boldsymbol{b}}_1$ of the body frame and define $\boldsymbol{s}_2$ in Equation (10). The third vector $\hat{s}_3$ of the $\mathcal{S}_1$ frame, is naturally created from the first two.

$$\hat{s}_2 = \frac{\hat{s}_1 \times \hat{b}_1}{|\hat{s}_1 \times \hat{b}_1|} \qquad \hat{s}_3 = \frac{\hat{s}_1 \times \hat{s}_2}{|\hat{s}_1 \times \hat{s}_2|} \tag{10}$$

The problem that arises is the singularity that occurs when $\hat{\boldsymbol{b}}_1$ and $\boldsymbol{d}$ become aligned: this frame becomes undefined. In order to counteract this, using a similar process as the shadow set used for Modified Rodrigues Parameters [11], a second frame is created. This frame $\mathcal{S}_2 = \{\hat{\tilde{s}}_1 = \hat{s}_1, \hat{\tilde{s}}_2, \hat{\tilde{s}}_3\}$ is created with the same first vector, but constructs $\hat{\tilde{s}}_2$ using $\hat{\boldsymbol{b}}_2$ of the body frame as in Equation (11). The last vector, once again, finishes the orthonormal frame.

$$\hat{\tilde{s}}_2 = \frac{\hat{\tilde{s}}_1 \times \hat{b}_2}{|\hat{\tilde{s}}_1 \times \hat{b}_2|} \tag{11}$$

With both these frames, $\mathcal{S}_1$ and $\mathcal{S}_2$, the singularities can always be avoided. Indeed, $\mathcal{S}_1$ becomes singular when $\boldsymbol{d}$ approches $\hat{\boldsymbol{b}}_1$, while $\mathcal{S}_2$ becomes singular when the sunheading approaches $\hat{\boldsymbol{b}}_2$. By changing frames, whenever the sunline gets within a safe cone of 30° (a modifiable value) of $\hat{\boldsymbol{b}}_1$, the frame is rotated into $\mathcal{S}_2$, which is not singular. Similarly, when $\boldsymbol{d}$ approches $\hat{\boldsymbol{b}}_2$ the frame is switched back to $\mathcal{S}_1$.

Because the two frames share the sunline vector $\boldsymbol{d}$, this vector is the same in both frames. This is a clear advantage as this is the vector we desire to estimate, and not having to rotate it avoids numerical issues. The rotation of the rates is done by computing the following DCMs, of which all the vectors are known.

$$[\mathcal{BS}_1] = \begin{bmatrix} {}^{\mathcal{B}}\hat{\boldsymbol{s}}_1 & {}^{\mathcal{B}}\hat{\boldsymbol{s}}_2 & {}^{\mathcal{B}}\hat{\boldsymbol{s}}_3 \end{bmatrix} \qquad [\mathcal{BS}_2] = \begin{bmatrix} {}^{\mathcal{B}}\hat{\hat{\boldsymbol{s}}}_1 & {}^{\mathcal{B}}\hat{\hat{\boldsymbol{s}}}_2 & {}^{\mathcal{B}}\hat{\hat{\boldsymbol{s}}}_3 \end{bmatrix} \qquad [\mathcal{S}_2\mathcal{S}_1] = [\mathcal{BS}_2]^T[\mathcal{BS}_1] \quad (12)$$

Filter Dynamics The filter is therefore derived with the states being $\boldsymbol{X} = \begin{bmatrix} {}^{\mathcal{B}}\boldsymbol{d} & \omega_2 & \omega_3 \end{bmatrix}^T$, given that $\boldsymbol{\omega}_{\mathcal{S}/\mathcal{B}} = {}^{\mathcal{S}}\begin{bmatrix} \omega_1 & \omega_2 & \omega_3 \end{bmatrix}^T$. The rates of $\mathcal{S}$ relative to the body and inertial frame are related as such: $\boldsymbol{\omega}_{\mathcal{S}/\mathcal{N}} - \boldsymbol{\omega}_{\mathcal{S}/\mathcal{B}} = \boldsymbol{\omega}_{\mathcal{B}/\mathcal{N}}$. Since ω_1 is unknown, it is set to zero. Furthermore, since the sun heading is considered to be constant in the inertial frame over the period of time required for attitude determination and control, the equation becomes $-\bar{\boldsymbol{\omega}}_{\mathcal{S}/\mathcal{B}} = \bar{\boldsymbol{\omega}}_{\mathcal{B}/\mathcal{N}}$.

$\boldsymbol{\omega}_{\mathcal{S}/\mathcal{B}}$ is estimated directly by the filter, and its skew matrix can be computed by setting ω_1 to zero (in the absence of information). This defines $\tilde{\boldsymbol{\omega}}_{\mathcal{B}/\mathcal{N}}$ as a function of known parameters. The dynamics are therefore given by Equations (13) and (14), where $[\tilde{\boldsymbol{d}}](2,3)$ corresponds to the 2nd and 3rd columns of the $[\tilde{\boldsymbol{d}}]$ matrix.

$$\boldsymbol{X}' = \boldsymbol{F}(\boldsymbol{X}) = \begin{bmatrix} {}^{\mathcal{B}}\boldsymbol{d}' \\ \omega_2' \\ \omega_3' \end{bmatrix} = \begin{bmatrix} -\bar{\boldsymbol{\omega}}_{\mathcal{B}/\mathcal{N}} \times {}^{\mathcal{B}}\boldsymbol{d} \\ 0 \\ 0 \end{bmatrix} = \begin{bmatrix} \begin{bmatrix} 0 \\ \omega_2 \\ \omega_3 \end{bmatrix} \times {}^{\mathcal{B}}\boldsymbol{d} \\ 0 \\ 0 \end{bmatrix} \quad (13)$$

$$[A] = \left[\frac{\partial \boldsymbol{F}(\boldsymbol{d}, t_i)}{\partial \boldsymbol{X}}\right] = \begin{bmatrix} [\tilde{\tilde{\boldsymbol{\omega}}}_{\mathcal{S}/\mathcal{B}}] & -[\tilde{\boldsymbol{d}}](2,3) \\ [0]_{2\times 3} & [0]_{2\times 2} \end{bmatrix} \quad (14)$$

This formulation leads to simple dynamics, much simpler than those of the filter which subtracts the unobservable states, yet can actually estimate the observable of the rate, instead of using past estimates of $\boldsymbol{d}$.

Switching Frames When switching occurs, the switch matrix W can be computed in Equation (15) using the previously computed DCMs. This equation assumes the switch is going from frame 1 to frame 2 (the reciprocal is equivalent), and $[\mathcal{S}_2\mathcal{S}_1](2,3)$ corresponds to the 2nd and 3rd columns of the $[\mathcal{S}_2\mathcal{S}_1]$ matrix.

$$[W] = \begin{bmatrix} [I]_{3\times 3} & [0]_{3\times 2} \\ [0]_{2\times 3} & [\mathcal{S}_2\mathcal{S}_1](2,3) \end{bmatrix} \quad (15)$$

The new states $\boldsymbol{X}$ and covariance [P] after the switch are therefore given in Equation (16)

$$\bar{\boldsymbol{X}} = [W]\boldsymbol{X} \qquad [\bar{P}] = [W][P][W]^T \quad (16)$$

When writing out the values of the state and covariance, it is necessary to bring it back into the body frame, using the $[\mathcal{BS}]$ DCM ($\mathcal{S}$ representing the current frame in use).

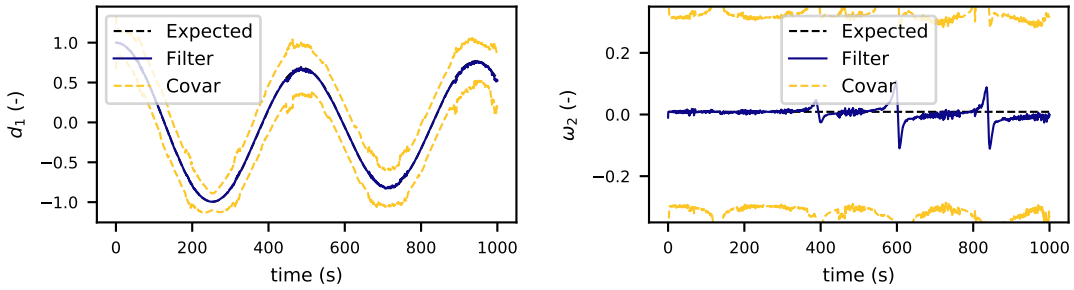

(a) First Heading Component (b) ω_2 Component

Figure 5. State Error and Covariance Plots for SunHeading components of Switch-EKF, FOV: 85°

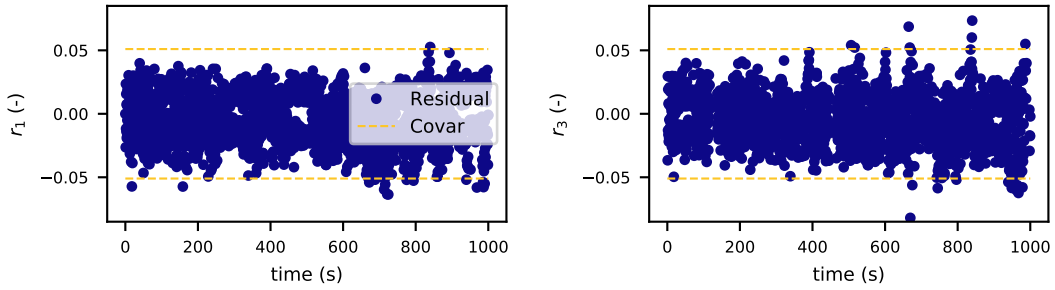

(a) First Active CSS (b) Third Active CSS

Figure 6. Post Fit Residuals for Switch-EKF, FOV: 85°

SIMULATION AND RESULTS

As described in the previous section, out of these 3 kinematic formulations, 4 filters were developed. The subtraction of the unobservable states formulation was written into a square-root unscented Kalman Filter (SR-uKF), and an Extended Kalman Filter (EKF). The formulation which only estimates the sunline direction was implemented in an EKF (Sunline-EKF), as well as the switch filter (Switch-EKF).

The simulation used was created using the Basilisk Software Package*[13].In all of the runs, a spacecraft is in deep space, at 1AU from the sun, tumbling. The problem assumes that the time needed for control is much smaller than the time needed to orbit around the Sun, meaning that $\dot{\boldsymbol{d}} = \mathbf{0}$. The satellite is therefore not put on orbit around the Sun, but kept in a constant location in the inertial frame. The simulations inputs are listed in Table 4. This frameworks allows for a fully coupled dynamic simulation, and the runs use the same physical scenario, with only the filters changing between runs. The average run-time over 50 conservative tests is also added in Table 2 for each of the filters. Although there are differences—notably due to the size of the state vector—speed is not the main discriminating factor in the comparison of filter performance. The uKF in its square-root implementation is faster than the EKF for the same filter formulation; this result is predicted by Reference [12].

*http://hanspeterschaub.info/bskMain.html

Table 2. Filter Run Times for 1000s Test Run

Filter	Sunline-EKF	EKF	SR-uKF	Switch-EKF
RunTime (s)	0.21	0.28	0.24	0.24

Table 3. Simulation Parameters

Parameter	$\boldsymbol{\sigma}(t_0)$	$\boldsymbol{\omega}(t_0)$ (°/s)	$[I]$ (kg/m^2)	Mass (kg)	simulation time (s)
Value	$[0,0,0]^T$	$[-0.1,0.5,0.5]^T$	diag(900,800,600)	750	1000

Table 4. Filter Initialization

Parameter	$\boldsymbol{X}(t_0)$	$[P](t_0)$	$[Q](\sigma_m = 0.017)$
Sunline-EKF	$[0,0.1,1]^T$	diag$(1,1,1)$	diag$(\sigma_m^2,\sigma_m^2,\sigma_m^2)$
EKF SR-uKF Switch-EKF	$[0,0.1,1,0.01,0.01,0]^T$	diag(1,1,1,0.02,0.02,0.02)	diag$(\sigma_m^2,\sigma_m^2,\sigma_m^2,\frac{\sigma_m^2}{100},\frac{\sigma_m^2}{100},\frac{\sigma_m^2}{100})$

Table 5. Post Fit Residuals, FOV: 85°

Filter	Statistics	Obs 1	Obs 2	Obs 3	Obs 4
Sunline-EKF	Means	0.0004	0.0	0.0	0.001
	Standard Deviations	0.0342	0.0207	0.0347	0.022
EKF	Means	-0.0012	-0.0015	-0.001	-0.0005
	Standard Deviations	0.0167	0.0165	0.0162	0.0165
SR-uKF	Means	-0.0	0.0004	0.0046	0.0162
	Standard Deviations	0.0226	0.036	0.0654	0.1002
Switch-EKF	Means	-0.0049	-0.0068	-0.004	-0.0063
	Standard Deviations	0.0254	0.0448	0.0455	0.02

CSS Field of View set to 85°

The first simulation runs the filters with good quality measurements. With a field of view of 85° on each sensor, the problem has good observability, as seen in Figures 2(b) and 3(b). Table 5 shows the post fit residuals' means and standard deviations for each of the activated devices. All the means are near zero, which indicates no biases. The standard deviations are sometimes a large, which is due to the first measurements, or sections with less activated CSSs. It can be noted that the EKF performs best in this realm.

These filters are compared by plotting their off-pointing in degrees and the norm of the error on $\boldsymbol{d}'$ in Figures 7. The data was smoothed using a Savitzky-Golay algorithm [14]. Figure 5 shows the Switch-EKF tracking the true states well despite a frequent jump in the rates. This plot only shows

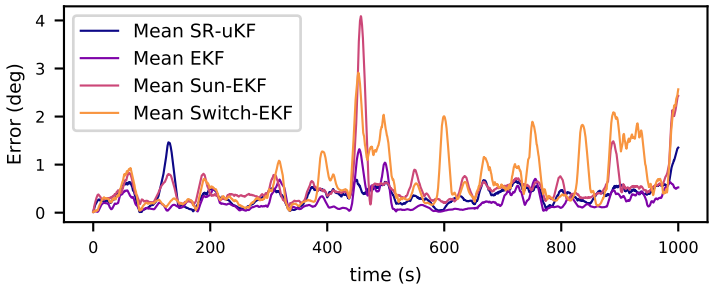

(a) Pointing Miss-Angle (°)

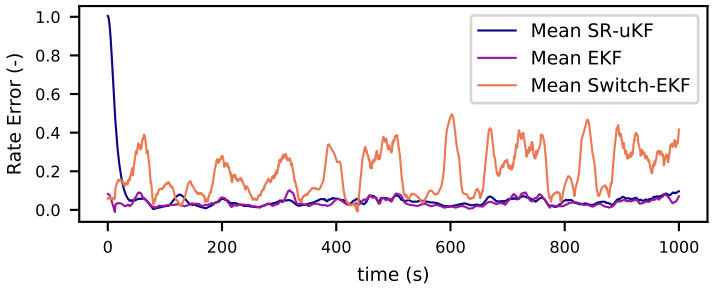

(b) $\boldsymbol{d}'$ norm error

Figure 7. Comparative performance of the filters, FOV: 85°

the first component of $\boldsymbol{d}$ and ω_2 as the other components are similar. The post fits are plotted in Figure 6, just for the first 2 active sensors (other post fits are similar). This filter, despite being the least performant, is still estimating the states well. The miss angle never goes significantly higher than $3°$, and the RMS errors all stay below $0.8°$. These RMS errors are summarized in Table 6. It is reminded in this table that the Sunline-EKF does not estimates rates, hence the absence of a curve in Figure 9(b), and the N/A in Table 6.

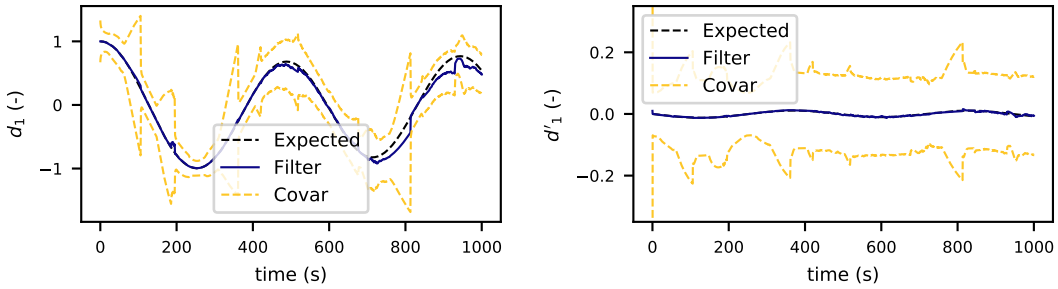

(a) First Heading Component

(b) $\boldsymbol{\omega}_2$ Component

Figure 8. State Error and Covariance Plots for SunHeading components of EKF, FOV: 60°

CSS Field of View set to 60°

The second simulation runs the filters assuming the devices have 60° FOV, emulating a lower-performance sensor. The observability can become problematic as seen in Figures 2(a) and 3(a).

Table 6. RMS Errors from Truth, FOV: 85°

Filter	Sunline-EKF	EKF	SR-uKF	Switch-EKF
$\boldsymbol{d}$ RMS Pointing Error (°)	0.611	0.277	0.394	0.767
$\boldsymbol{d}'$ RMS Error (-)	N/A	0.037	0.04	0.213

Table 7. RMS Errors from Truth, FOV: 60°

Filter	Sunline-EKF	EKF	SR-uKF	Switch-EKF
$\boldsymbol{d}$ RMS Pointing Error (°)	14.469	5.092	3.811	28.398
$\boldsymbol{d}'$ RMS Error (-)	N/A	0.101	0.089	1.276

Despite an overall dip in performance, the EKF and the SR-uKF seem to be the most resilient to the poorer sensors. This is seen more thoroughly in Table 7 and in Figure 9.

These filters are compared by plotting their off-pointing in degrees and the norm of the error on $\boldsymbol{d}'$ in Figures 9. Figure 8 shows the EKF tracking the true states well. In this scenario, only the EKF and the SR-uKF perform well. The Sunline-EKF and the Switch-EKF have large miss-angles. Although there is a stark increase in errors even for the EKF and SR-uKF, which both use the same formulation, they are still within 6° of error on average. These RMS errors are summarized in Table 7, while the EKF and SR-uKF are compared in Figure 9.

CONCLUSIONS

This paper has shown the comparative performances of several filters and formulations attempting to solve the CSS-only attitude determination problem. The subtraction of the unobservable states seem to perform the best all around, whether the CSS have a narrow or wide field of view. In the case of lower observability, the square-root uKF outperforms the EKF, which is not surprising due to its better propagation step. The Sunline-EKF, which does not estimate rate, but only computes it using past sun heading estimates, does not do as good with state estimation, especially when the sensors are providing less measurements.

The switch-EKF, which tracks these two frames did not perform as well as expected. It has a more non-linear formulation, and therefore could need to be implemented in a uKF or SR-uKF for better performance. Although it's the preferred formulation and derivation, it must perform better before being considered for long-term implementation. Despite this, when sun-sensors provide many measurements (in the case of a $85°$ FOV), it does not perform worse than the other filters presented here. Its formulation does decouple the unobservable rate component, and therefore provides a step towards CSS-only filters that can be used during safe-mode.

REFERENCES

[1] S. Allgeier, M. Mahin, and N. Fitz-Coy, *Design and Analysis of a Coarse Sun Sensor for Pico-Satellites*. American Institute of Aeronautics and Astronautics, 2017/12/19 2009, doi:10.2514/6.2009-1837.

[2] W.-T. C. T. C. Fu-Yuen Hsiao and C. Rebelo, *Coarse Sun Acquisition Only with Sun Sensors for Micro Satellites*. AAS 15-319, 2015.

[3] S. S. M. Swei, J. C. Fusco, and R. H. Nakamura, "Design of Sun-Safe Controllers for Lunar Atmosphere and Dust Environment Explorer," *Journal of Guidance, Control, and Dynamics*, Vol. 39, 2017/12/19 2016, pp. 2022–2033, 10.2514/1.G000270.

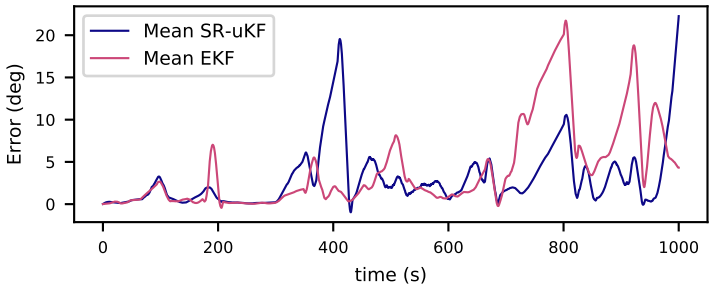

(a) Pointing Miss-Angle (°)

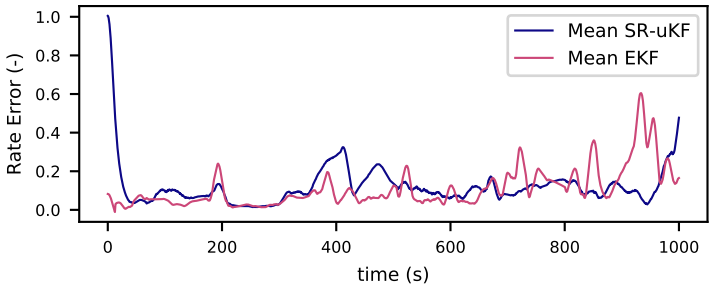

(b) $\boldsymbol{d}'$ norm error

Figure 9. Comparative performance of the EKF and SR-uKF, FOV: 60°

[4] J. Fusco, S. S.-M. Swei, and R. Nakamura, *Sun Safe Mode Controller Design for LADEE*. American Institute of Aeronautics and Astronautics, 2017/12/19 2015, doi:10.2514/6.2015-2011.

[5] S. A. O'Keefe and H. Schaub, "Gyro Accuracy and Failure Sensitivity of Underdetermined Coarse Sun Heading Estimation," *AAS/AIAA Space Flight Mechanics Meeting*, Williamsburg, VA, Jan. 11–15 2015. Paper AAS 15-344.

[6] S. A. O'Keefe and H. Schaub, "Sun Heading Estimation using Underdetermined Set of Coarse Sun Sensors," *AAS/AIAA Astrodynamics Specialists Conference*, Hilton Head, SC, Aug. 11–15 2013. Paper No. AAS-13-891.

[7] R. Y. Chiang and T. Tsao, *Gyroless 3-Axis Sun Acquisition via Sun Sensors Only Unscented Kalman Filter Estimation*. American Institute of Aeronautics and Astronautics, 2017/12/19 2013, doi:10.2514/6.2013-5025.

[8] T. Tsao and R. Chiang, *Gyroless Transfer Orbit Sun Acquisition Using Only Wing Current Feedback*. American Institute of Aeronautics and Astronautics, 2017/12/19 2009, doi:10.2514/6.2009-5944.

[9] S. A. O'Keefe and H. Schaub, "On-Orbit Coarse Sun Sensor Calibration Sensitivity to Sensor and Model Error," *AAS/AIAA Space Flight Mechanics Meeting*, Williamsburg, VA, Jan. 11–15 2015. Paper AAS 15-392.

[10] B. S. B. Tapley and G. Born, *Statistical Orbit Determination*. No. ISBN 9780126836301, Elsevier Academic Press, 2004.

[11] H. Schaub and J. L. Junkins, *Analytical Mechanics of Space Systems*. Reston, VA: AIAA Education Series, 3rd ed., 2014, 10.2514/4.102400.

[12] R. v. d. Merwe, "The Square-Root Unscented Kalman Filter for State and Parameter-Estimation," Acoustics, Speech, and Signal Processing, 2001.

[13] J. Alcorn and H. Schaub, "Simulating Attitude Actuation Options Using the Basilisk Astrodynamics Software Architecture," *67th International Astronautical Congress*, Guadalajara, Mexico, Sept. 26–30 2016.

[14] A. Savitzky and M. J. E. Golay, "Smoothing and Differentiation of Data by Simplified Least Squares Procedures," *Analytical Chemistry*, Vol. 36 (8), July 1964, pp. 1627–1639.